The Cryosphere Discuss., doi:10.5194/tc-2016-38, 2016
Manuscript under review for journal The Cryosphere
Published: 4 March 2016

The Cryosphere Discussions

An investigation of the thermo-mechanical features of Laohugou Glacier No.12 in Mt. Qilian Shan, western China, using a two-dimensional first-order flow-band ice flow model

Yuzhe Wang[1,2], Tong Zhang[3], Jiawen Ren[1], Xiang Qin[1], Yushuo Liu[1], Weijun Sun[4], Jizu Chen[1,2], Minghu Ding[3], Wentao Du[1,2], and Dahe Qin[1]

[1]State Key Laboratory of Cryospheric Sciences, Cold and Arid Regions Environmental and Engineering Research Institute, Chinese Academy of Sciences, Lanzhou 730000, China
[2]University of Chinese Academy of Sciences, Beijing 100049, China
[3]Insititute of Climate System & Polar Meteorology, Chinese Academy of Meteorological Sciences, Beijing 100081, China
[4]College of Geography and Environment, Shandong Normal University, Jinan 250014, China

Correspondence to: Tong Zhang (tzhang@camscma.cn)

Abstract. En-glacial thermal conditions are very important for controlling ice rheology. By combining *in situ* measurements and a two-dimensional thermo-mechanically coupled ice flow model, we investigate the present thermal status of the largest valley glacier (Laohugou No.12; LHG12) in Mt. Qilian Shan in the arid region of western China. Our model results suggest that LHG12, previously considered as fully cold, is probably polythermal, with a lower temperate ice layer (approximately 5.4 km long) overlain by an upper layer of cold ice over a large region of the ablation area. Generally, modelled ice surface velocities match *in situ* observations in the east branch (mainstream) well but clearly underestimate the ice surface velocities near the glacier terminus because the convergent flow of the west branch is ignored. The modelled ice temperatures agree closely with the *in situ* measurements (with biases less than 0.5 K) from a deep borehole (110 m) in the upper ablation area. The model results were highly sensitive to surface thermal boundary conditions, for example, surface air temperature and near-surface ice temperature. In this study, we suggest using a combination of surface air temperatures and near-surface ice temperatures (following the work of Wohlleben et al., 2009) as Dirichlet surface thermal conditions to include the contributions of the latent heat released during refreezing of surface melt-water in the accumulation zone. Like many other alpine glaciers, strain heating is the most important parameter controlling the en-glacial thermal structure in LHG12.

1 Introduction

The storage of water in glaciers is an important component of the hydrological cycle at different time scales (Jansson et al., 2003; Huss et al., 2010), especially in arid and semi-arid regions such as northwestern China, where many glaciers are currently retreating and disappearing (Yao et al., 2012; Neckel et al., 2014; Tian et al., 2014). As a very important water source for the inhabitants of northwestern China, Mt. Qilian Shan (MQS), which is located on the northeastern edge of the Tibetan Plateau (36 – 39 °N, 94 – 104 °E), develops approximately 2051 glaciers that cover an area of approximately 1057 km^2 and have a

The Cryosphere Discuss., doi:10.5194/tc-2016-38, 2016
Manuscript under review for journal The Cryosphere
Published: 4 March 2016

total ice volume of approximately 50.5 km^3 (Guo et al., 2014, 2015). Thus, the changes in the MQS glaciers that occur as the climate becomes warmer in the near future are of concern.

Due to logistic difficulties, few MQS glaciers have been investigated in previous decades. However, Laohugou Glacier No.12 (hereafter referred to as LHG12), the largest valley glacier of MQS, has been investigated. Comprised of two branches (east and west), LHG12 is located on the north slope of western MQS (39°27’ N, 96°32’ E; Fig. 1), with a length of approximately 9.8 km, an area of approximately 20.4 km^2, and an elevation range of 4260 – 5481 m a.s.l. (Liu et al., 2011). LHG12 was first studied by a Chinese expedition from 1958 – 1962 and was considered again in short-term field campaigns in the 1970s and 1980s that were aimed at monitoring glacier changes (Du et al., 2008). Since 2008, the Chinese Academy of Sciences has operated a field station for obtaining meteorological and glaciological measurements of LHG12.

The temperature distribution of a glacier primarily controls the ice flow rheology, en-glacial hydrology, and basal sliding conditions of the glacier (Blatter and Hutter, 1991; Irvine-Fynn et al., 2011; Schäfer et al., 2014). For example, the existence of basal temperate ice was responsible for modelled velocity biases in a first-order model when compared with the “full” Stokes modelling approach (Zhang et al., 2015). In addition, the thermal regime of a glacier can be strongly influenced by the surface thermal boundary conditions. For example, near-surface warming from refreezing melt-water and cooling from the cold air of crevasses influence the thermal regimes of glaciers (Wilson and Flowers, 2013; Wilson et al., 2013; Meierbachtol et al., 2015). Using both *in situ* measurements and numerical models, Meierbachtol et al. (2015) argued that shallow borehole ice temperatures served as better boundary constraints than surface air temperatures in Greenland. However, for the east Rongbuk glacier on Mt. Everest, which is considered polythermal, Zhang et al. (2013) found that the modelled ice temperatures agreed well with the *in situ* shallow borehole observations when using surface air temperatures as the surface thermal boundary condition. Therefore, careful investigation of the upper thermal boundary condition is highly necessary for glaciers in different regions under different climate conditions.

LHG12 is widely considered as an extremely continental-type (cold) glacier and is characterized by low temperatures and precipitation (Huang, 1990; Shi and Liu, 2000). However, in recent years, we have observed extensive and widespread melt-water at the ice surfaces and glacier terminus. In addition, percolation of snow melt-water consistently occurs in the accumulation basin during the summer. Therefore, we address the following two pressing questions in this study: (i) What is the present thermal status of LHG12? and (ii) How do different surface thermal boundary conditions impact the modelled ice temperature and flow fields? Because warm ice can assist basal slip and accelerate glacier retreat, understanding the current thermal status of LHG12 is very important for predicting its future dynamic behaviour.

To answer these questions, we conduct diagnostic simulations for LHG12 by using a thermo-mechanically coupled first-order flow-band ice flow model. This paper is organized as follows: First, we provide a detailed description of the glaciological dataset of LHG12. Then, we briefly review the numerical ice flow model used in this study. After performing a set of model sensitivity experiments, we compare the model results with the measured ice surface velocities and the ice temperature profile obtained from a deep borehole. Next, we investigate the impacts of different thermal surface boundary conditions and assess the contributions of heat advection, strain heating, and basal sliding to the temperature field of LHG12. Finally, we discuss the limitations of our model and present the important conclusions that resulted from this study.

The Cryosphere Discuss., doi:10.5194/tc-2016-38, 2016
Manuscript under review for journal The Cryosphere
Published: 4 March 2016

2 Field data

Most *in situ* observations, e.g., borehole ice temperatures, surface air temperatures and ice surface velocities, have been made on the east branch (mainstream) of LHG12 (Fig. 1). Measurements on the west branch are dispersed and temporally discontinuous. Thus, we only consider the *in situ* data from the east tributary when building our numerical ice flow model.

2.1 Glacier geometry

In July – August 2009 and 2014, two ground-penetrating radar (GPR) surveys were conducted on LHG12 using a pulseEKKO PRO system with center frequencies of 100 MHz (2009) and 50 MHz (2014) (Fig. 1). Wang et al. (in press) have presented details regarding the GPR data collection and post-processing.

As shown in Fig. 2a, the east branch of LHG12 has a mean ice thickness of approximately 190 m. We observed the thickest ice layer (approximately 261 m) at 4864 m a.s.l. Generally, the ice surface of LHG12 is gently undulating, with a mean slope of 0.08, and the bed of LHG12 shows significant over-deepening in the middle of the center flow-line (CL) (Fig. 2a). The transverse profiles of the glacier can be described by the power law function $d = aL^b$, where d and L are the vertical and horizontal distances from the lowest point of the profile, and a and b are constants that represent the flatness and steepness of the glacier valley, respectively (Svensson, 1959). The b values for LHG12 range from 0.8 to 1.6, indicating that the valley containing LHG12 is approximately "V"-shaped (Wang et al., in press). As an input for the flow-band ice flow model, the glacier width, W, was also calculated by ignoring all tributaries (including the west branch) (Fig. 1 and 2b).

2.2 Ice surface velocities

The surface velocities of the ice in LHG12 were determined from repeated surveys of stakes drilled into the ice surface. All stakes were located in an elevation span of 4355 – 4990 m.a.s.l. (Fig. 1). We measured the stake positions using a real-time kinematic (RTK) method by a South Lingrui S82 GPS system (Liu et al., 2011). Because it is difficult to conduct fieldwork on LHG12 (due to, e.g., crevasses and supra-glacial streams), it was nearly impossible to measure all stakes each observational year. Thus, the current dataset includes annual ice surface velocities from 2008 – 2009 and 2009 – 2010, summer measurements from June 17 – August 30, 2008, and winter measurements from February 1 – May 28, 2010.

The *in situ* ice surface velocities shown in Fig. 3 are all from stakes near the CL (Fig. 1). Small ice surface velocities ($<$ 17 m a^{-1}) are clearly visible in the upper accumulation (km 0 – 1.2) and lower ablation areas (km 6.5 – 9.0) (Fig. 3). Fast ice flow ($>$ 30 m a^{-1}) can be observed between elevations of 4700 – 4775 m a.s.l. (km 4.0 – 5.0), where the ice surface velocities during the summer are approximately 6 m a^{-1} greater than the annual mean velocity ($<$ 40 m a^{-1}). Measurements of winter ice surface velocities ($<$ 10 m a^{-1}) are only available near the glacier terminus showing a clear inter-annual variation of ice speed.

The Cryosphere Discuss., doi:10.5194/tc-2016-38, 2016
Manuscript under review for journal The Cryosphere
Published: 4 March 2016

2.3 Surface air temperature

Two automatic weather stations (AWS) were deployed on LHG12, one in the ablation area at 4550 m a.s.l. (site 1, see Fig. 1), and one in the accumulation area at 5040 m a.s.l. (site 3). During the period of 2010 – 2013, the mean annual air temperatures (2 m above the ice surface) at sites 1 and 3 were $-9.2\,^{\circ}\mathrm{C}$ and $-12.2\,^{\circ}\mathrm{C}$, respectively, suggesting a lapse rate of -0.0061 K m^{-1}. These results were used to calculate the distribution of the surface air temperatures at all elevations on LHG12.

2.4 Borehole ice temperature

In August 2009 and 2010, we drilled three 25m deep shallow boreholes (Fig. 1). One borehole was drilled in the upper ablation area (site 2, approximately 4900 m a.s.l.) and two boreholes were drilled at the AWS locations (sites 1 and 3). The snow/ice temperatures were measured at the boreholes during the period of October 1, 2010 – September 30, 2011. The seasonal variations of the snow/ice temperatures in the shallow boreholes are presented in Figs. 4a, b and c. Our measurements show very little fluctuation ($\pm$0.4 K) in the ice temperatures over the depth range of 20 – 25 m. Below the 3 m depth, the annual mean temperature profiles for sites 1 and 2 show a linearly increase in temperature with depth, while the annual mean temperature profile for site 3 is convex upward. The mean annual ice temperatures at a depth of 20 m (T_{20m}) at sites 1, 2, and 3 are 5.5 K, 3.0 K and 9.5 K higher than the mean annual air temperatures (T_{air}), respectively. Despite its higher elevation, the near-surface snow/ice temperatures below a depth of 5 m at site 3 are greater than the near-surface snow/ice temperatures in the ablation area (sites 1 and 2), largely due to the latent heat released as the melt-water entrapped in the surface snow layers refreezes, as observed in many previous field expeditions.

To determine the en-glacial thermal conditions of LHG12, we drilled a deep ice core (167 m) in the lower accumulation area of LHG12 (approximately 4971 m a.s.l., Fig. 1). Ice temperature data were obtained to a depth of approximately 110 m, as shown in Fig. 4d. We can clearly see that the ice temperature largely increases from -10 °C at the surface to -6 °C at the depth of 4 m. At the depth of 9 m, the ice temperature lowers to a minimum value of -6.6 °C. In the range of 9 m – 30 m depth, the temperature profile is close to linear with a temperature gradient of about +0.1 K m^{-1}. Below the depth of 30 m, the ice temperature also demonstrates a linear relationship with depth but with a smaller temperature gradient of about +0.034 K m^{-1}.

3 Model description

In this study, we used the same two-dimensional (2D), thermo-mechanically coupled, first-order, flow-band ice flow model as Zhang et al. (2013). Therefore, we only address a very brief review of the model here.

3.1 Ice flow model

We define x, y and z as the horizontal along-flow, horizontal across-flow and vertical coordinates, respectively. The glacier force balance equation is given as follows:

$$\frac{\partial}{\partial x}(2\sigma'_{xx}+\sigma'_{yy})+\frac{\partial \sigma'_{xy}}{\partial y}+\frac{\partial \sigma'_{xz}}{\partial z}=\rho g\frac{\partial s}{\partial x}, \tag{1}$$

The Cryosphere Discuss., doi:10.5194/tc-2016-38, 2016
Manuscript under review for journal The Cryosphere
Published: 4 March 2016

where σ'_{ij} is the deviatoric stress tensor, ρ is the ice density, g is the gravitational acceleration and s is the ice surface elevation. The parameters used in this study are given in Table 1.

The constitutive relationship of ice dynamics is described by the Glen's flow law as follows (Cuffey and Paterson, 2010):

$$\sigma'_{ij} = 2\eta\dot{\epsilon}_{ij}, \quad \eta = \frac{1}{2}A^{-1/n}(\dot{\epsilon_e} + \dot{\epsilon}_0)^{(1-n)/n}, \tag{2}$$

where η is the ice viscosity, $\dot{\epsilon}_{ij}$ is the strain rate, n is the flow law exponent, A is the flow rate factor, $\dot{\epsilon_e}$ is the effective strain rate, and $\dot{\epsilon}_0$ is a small number used to avoid singularity. The flow rate factor is parameterized using the Arrhenius relationship as follows:

$$A(T) = A_0 \exp(-\frac{Q}{RT}), \tag{3}$$

where A_0 is the pre-exponential constant, Q is the activation energy for creep, R is the universal gas constant and T is the ice temperature. The effective strain rate is related to the velocity gradient as follows:

$$\dot{\epsilon}_e^2 \simeq \left(\frac{\partial u}{\partial x}\right)^2 + \left(\frac{\partial v}{\partial y}\right)^2 + \frac{\partial u}{\partial x}\frac{\partial v}{\partial y} + \frac{1}{4}\left(\frac{\partial u}{\partial y}\right)^2 + \frac{1}{4}\left(\frac{\partial u}{\partial z}\right)^2, \tag{4}$$

where u and v are the velocity components along the x and y direction, respectively. By assuming $\partial v/\partial y = (u/W)(\partial W/\partial x)$, we parameterize the lateral drag, σ_{xy}, as a function of the flow-band half width, W, as follows (Flowers et al., 2011):

$$\sigma_{xy} = -\frac{\eta u}{W}. \tag{5}$$

3.2 Ice temperature model

The 2D temperature model, where the horizontal diffusion is parameterized by glacier width, is given by

$$k\left(\frac{\partial^2 T}{\partial x^2} + \frac{1}{W}\frac{\partial W}{\partial x}\frac{\partial T}{\partial x} + \frac{\partial^2 T}{\partial z^2}\right) - \rho c_p\left(u\frac{\partial T}{\partial x} + w\frac{\partial T}{\partial z}\right) + 4\eta\dot{\epsilon_e}^2 = 0, \tag{6}$$

where k and c_p are the thermal conductivity and heat capacity of the ice, respectively.

The pressure melting point of the ice, T_{pmp}, is described by the Clausius-Clapeyron relationship as follows:

$$T_{\text{pmp}} = T_0 - \beta(s - z), \tag{7}$$

where T_0 is the triple-point temperature of water and β is the Clausius-Clapeyron constant. Following Zhang et al. (2013), we determined the position of the cold-temperate ice transition surface (CTS) by considering the following two cases: (i) melting condition, i.e., cold ice flows downward into the temperate ice zone, and (ii) freezing condition, i.e., temperate ice flows upward into the cold ice zone (Blatter and Hutter, 1991; Blatter and Greve, 2015). For the melting case, the ice temperature profile at the CTS simply follows a Clausius-Clapeyron gradient (β). However, for the freezing case, the latent heat, Q_r, that is released when the water contained in the temperate refreezes is determined as follows (Funk et al., 1994):

$$Q_r = w\omega\rho_w L, \tag{8}$$

The Cryosphere Discuss., doi:10.5194/tc-2016-38, 2016
Manuscript under review for journal The Cryosphere
Published: 4 March 2016

where ω is the fractional water content of the temperate ice, ρ_w is the water density and L is the latent heat of freezing. In this case, the ice temperature gradient at the CTS can be described as follows (Funk et al., 1994):

$$\frac{\partial T}{\partial z} = -\frac{Q_r}{k} + \beta. \tag{9}$$

3.3 Boundary conditions

In the ice flow model, we assume a stress-free condition for the glacier surface, and use the Coulomb friction law to describe the ice-bedrock interface where the ice slips (Schoof, 2005).

$$\tau_b = \Gamma\left(\frac{u_b}{u_b + \Gamma^n N^n \Lambda}\right)^{1/n} N, \qquad \Lambda = \frac{\lambda_{\max} A}{m_{\max}}, \tag{10}$$

where τ_b and u_b are the basal drag and velocity, respectively, N is the basal effective pressure, $\lambda_{\max}$ is the dominant wavelength of the bed bumps, $m_{\max}$ is the maximum slope of the bed bumps, and Γ and Λ are geometrical parameters (Gagliardini et al., 2007). The basal effective pressure, N, is defined as follows:

$$N = \rho g H - P_w = \phi \rho g H, \tag{11}$$

where H and P_w are the ice thickness and basal water pressure, respectively, and ϕ implies the ratio of basal effective pressure to the ice overburden pressure. The basal drag is defined as the sum of all resistive forces (Van der Veen, 1989; Pattyn, 2002).

We apply a Dirichlet temperature constraint (T_{sbc}) on the ice surface in the temperature model. In some studies, $T_{\text{sbc}} = T_{\text{air}}$ is used (e.g. Zhang et al., 2013), which, as suggested by recent studies, could result in lower velocity values (Sugiyama et al., 2014) and cold bias in ice temperature simulations (Meierbachtol et al., 2015). By contrast, Meierbachtol et al. (2015) recommended using the snow/ice temperature at the depth where inter-annual variations of air temperatures are damped (15 – 20 m, T_{dep}) (a proxy for the annual mean ice surface temperature). One advantage of using T_{dep} is that the effects of refreezing melt-water and the thermal insulation of winter snow can be included in the model (Huang et al., 1982; Cuffey and Paterson, 2010). In fact, the condition $T_{\text{dep}} = T_{\text{air}}$ is acceptable only in dry and cold snow zones (Cuffey and Paterson, 2010); however, $T_{\text{dep}} > T_{\text{air}}$ is often observed in zones where melt-water is refreezing in glaciers, such as the LHG12 glacier (Fig. 4). When including the impacts of ice advection, Wohlleben et al. (2009) suggested using a mean value of T_{dep} and T_{air} for the ablation surface. In this study, we adopt the method presented by Wohlleben et al. (2009) by setting

$$T_{\text{sbc}} = \begin{cases} T_{\text{20m}}, & \text{in the accumulation zone,} \\ (T_{\text{20m}} + T_{\text{air}})/2, & \text{in the ablation zone,} \end{cases} \tag{12}$$

which is denoted as a reference experiment (E-ref) after comparing the other two numerical experiments by setting $T_{\text{sbc}} = T_{\text{air}}$ (E-air) and $T_{\text{sbc}} = T_{\text{20m}}$ (E-20m) (see Sect. 4.3 for details). The T_{sbc} values in the ablation area are parameterized as a linear function of elevation and the environmental lapse rate using the measurements from sites 1 and 2, and all T_{sbc} values in the accumulation basin are set to T_{20m} for site 3.

At the ice-bedrock interface, we apply the following Neumann-type boundary condition in the temperature model:

$$\frac{\partial T}{\partial z} = -\frac{G}{k}, \tag{13}$$

The Cryosphere Discuss., doi:10.5194/tc-2016-38, 2016
Manuscript under review for journal The Cryosphere
Published: 4 March 2016

The Cryosphere Discussions
Open Access

where G is the geothermal heat flux . We here use a constant geothermal heat flux, 40 mW m^{-2}, an *in situ* measurement from the Dunde ice cap in the western MQS (Huang, 1999), over the entire model domain.

4 Model results and discussions

To understand the present thermal status of LHG12, we assume a thermal steady-state condition and perform a series of thermo-mechanically coupled diagnostic simulations using a 2D first-order flow-band model (described in above). First, we simulate the ice velocity and temperature fields for LHG12 by investigating the sensitivities of the model to geometrical bed parameters (λ_{max} and m_{max}), water content (ω), geothermal heat flux (G) and the valley shape index (b). Then, we inspect three different surface thermal boundary conditions (E-ref, E-air and E-20m) by comparing their model outputs with *in situ* ice temperature observations in the deep borehole at site 3. In addition, we perform four experiments (E-advZ, E-advX, E-strain, E-slip) to investigate the impacts of heat advection, strain heating and basal sliding on the thermal field and flow characteristics of LHG12.

4.1 Parameter sensitivity

As shown in Figs. 5 and 6, we conduct a series of sensitivity experiments to investigate the relative importance of different model parameters on ice flow speeds and temperate ice zone (TIZ) sizes by varying the value of one parameter while holding the other parameters fixed.

The friction law parameters, λ_{max} and m_{max}, which describe the geometries of bedrock obstacles (Gagliardini et al., 2007; Flowers et al., 2011), have non-negligible impacts on the model results. As shown in Figs. 5a and b, the modelled velocities and TIZ sizes increase as λ_{max} increases and m_{max} decreases, similar to in the results observed by Flowers et al. (2011) and Zhang et al. (2013). A large increase in the modelled velocity occurs when $m_{\text{max}} < 0.2$. The ratio, ϕ, is an insensitive parameter in our model when it is larger than 0.3 (Fig. 5c). Although the water content, ω, in the ice does not directly impact the ice velocity simulations (the flow rate factor A is assumed independent of the water content in ice), the water content can affect the temperature field and, consequently, influence A and the ice velocities (Fig. 5d). From Fig. 6d, we can clearly see that increasing the water content may result in larger TIZ sizes. For example, changing the water content from 1% to 3% nearly doubles the TIZ thickness over a horizontal distance of km 3.5 – 5.8. In addition, we test the sensitivity of the model to different geothermal heat flux values. A larger geothermal heat flux can result in larger TIZs but has a limited impact on modelling ice velocity (Figs. 5e and 6e). As shown by Zhang et al. (2013), our model results are mainly controlled by the shape of the glacial valley, specifically the b index (see Sect. 2.1). A large value of b indicates a flat glacial valley and suggests that a small lateral drag was exerted on the ice flow (Figs. 5f and 6f).

Based on the sensitivity experiments described above, we adopt a parameter set of $\lambda_{\text{max}} = 4$ m, $m_{\text{max}} = 0.3$, $\phi = 1$ (no basal water pressure), $\omega = 3\%$, $G = 40$ mW m^{-2} and $b = 1.2$ as a diagnostic reference in our modelling experiment (E-ref).

The Cryosphere Discuss., doi:10.5194/tc-2016-38, 2016
Manuscript under review for journal The Cryosphere
Published: 4 March 2016

4.2 Comparison with *in situ* observations

In the reference experiment (E-ref), we simulate the distributions of horizontal ice velocities and temperatures (Figs. 7a and c). Next, the model results are compared with the measured ice surface velocities and the ice temperature profile in the deep borehole (Figs. 7b and d). Generally, the modelled ice surface velocities agree well with *in situ* observations from the glacier head to km 5.3 along the CL (Fig. 7b). However, from 5.3 km to the glacier terminus, our model generally underestimates the ice surface velocity because the convergent flow from the west branch is ignored (Fig. 1), as shown in all of the simulations in Fig. 5. The basal sliding velocities are less than 4 m a^{-1} and contribute less than 10% to the mean annual ice surface velocities.

We observed a TIZ overlain by cold ice over a horizontal distance of km 1.1 – 6.5 (Fig. 7c). In addition, we further validated our numerical model by using *in situ* 110m deep ice temperature measurements (Fig. 7d). In this study, we use a 2D model approach that neglects ice flows and heat fluxes along the y direction. Consequently, it is very difficult to obtain numerical temperature results that agree perfectly with the *in situ* observations. However, as shown in Fig. 7d, a close match can be found between the model results and *in situ* measurements at depths of approximately 20 – 40 m and 80 – 90 m. The model overestimates the ice temperatures at depths of approximately 50 – 70 m and underestimates the ice temperatures at depths of approximately 100 – 110 m (by less than 0.5 K). Because *in situ* ice temperature data from below 110 m have not been obtained, we were unable to compare the modelled and measured ice temperatures at the ice-bedrock interface.

4.3 Choice of surface thermal boundary condition

We conduct three different numerical experiments (E-air, E-20m, and E-ref) to investigate the impacts of different surface thermal boundary conditions on the thermo-mechanical field of LHG12. For the E-air and E-20m experiments, we set $T_{\text{sbc}} = T_{\text{air}}$ and $T_{\text{sbc}} = T_{\text{20m}}$, respectively. E-ref was adopted in our "real" LHG12 simulations, which uses the T_{20m} in the accumulation basin and the $(T_{\text{20m}}+T_{\text{air}})/2$ in the ablation area, where the T_{20m} values below the equilibrium line altitude (ELA; approximately 4980 m a.s.l.) are linearly interpolated based on the *in situ* T_{20m} measurements at sites 1 and 2 (Fig. 4).

The intercomparison results of E-air, E-20m and E-ref for ice velocities and temperatures are presented in Fig. 8. The ice temperatures along the CL are highly sensitive to T_{sbc}. From E-air, it is observed that LHG12 becomes fully cold, with an average field temperature 5.7 K colder than that of E-ref (Fig. 8a), which decreases the ice surface velocity by approximately 13.5 m a^{-1} (Fig. 8b). Compared with E-ref, E-20m results in larger T_{sbc} values in the ablation area, greater mean ice temperatures (by approximately 1.0 K (Fig. 8a)), greater TIZ thicknesses (by approximately 5 m over a region of km 4.0 – 6.0 (Fig. 8c)), and faster ice surface velocities (by approximately 2 m a^{-1} (Fig. 8b)). Next, we compare the ice temperature modelling results with the *in situ* observations of the deep borehole at site 3 (Fig. 8d). E-ref results in the best simulation results, and E-20m, though generally similar to E-ref, generates warmer ice above a depth of 80 m in the deep borehole. Unsurprisingly, E-air results in an unreliable temperature profile that is colder than the actual temperatures at all depths.

As noted in above, the dynamics of LHG12 can be strongly influenced by the choices of different surface thermal boundary conditions. For LHG12, most accumulation and ablation events overlap during the summer season (Sun et al., 2012). The melt-water entrapped in snow and moulins during the summer season can release large amounts of heat due to refreezing when the temperature decreases, which may significantly increase the ice temperatures in the near-surface snow/ice layers (Fig. 4) and result in the warm bias of $T_{20\mathrm{m}}$ (compared with the mean annual surface air temperature). Therefore, compared with E-air, the E-ref and E-20m experiments better incorporate the effects of melt-water refreezing in the accumulation basin into the prescribed surface thermal boundary constraints resulting in more accurate simulations of ice temperature and flow fields.

4.4 Roles of heat advection, strain heating and basal sliding

To assess the relative contributions of heat advection and strain heating to the thermo-mechanical field of LHG12, we conducted three experiments (E-advZ, E-advX and E-strain), in which the vertical advection, horizontal along-flow advection and strain heating were “removed”, respectively. In addition, to investigate the effects of basal sliding predicted by the Coulomb friction law on the thermal state and flow dynamics of LHG12, we performed an experiment (E-slip) with $u_b = 0$.

Fig. 9 compares the ice velocity and temperature results of E-advZ, E-advX, E-strain and E-slip with those of E-ref. If the vertical advection is “dropped” (E-advZ; cold ice at the glacier surface cannot be transported downwards into the interior of LHG12), LHG12 becomes warmer (Figs. 9a and c) and flows faster relative to other experiments (Fig. 9b). As described for the discontinuous surface thermal boundary conditions across the ELA (a straightforward result from the refreezing of melt-water in the accumulation basin), a discontinuous transition of the mean column ice temperature was observed along the CL at km 1.3 (the horizontal position of ELA) in E-advX (Fig. 9a). Compared with E-ref, the E-advX experiment predicted colder field temperatures (by approximately 2.4 K) and much smaller surface ice velocities ($<$ 18 m a^{-1}). Because the accumulation basin of LHG12 is relatively warm, E-advX, which “removes” the horizontal transport of ice from upstream and downstream, predicted much colder conditions for LHG12, i.e., the modelled temperate ice only appears at three discontinuous grid points (Fig. 9c). As described by Zhang et al. (2015), we observed that strain heating contributes the most to the thermal configuration of LHG12. If we “remove” the strain heating (E-strain), LHG12 becomes fully cold, with a mean ice temperature field lower than that of E-ref by approximately 0.85 K. Consequently, the E-strain experiment predicts lower ice surface velocities (Fig. 9b). Previous studies have suggested that basal sliding can significantly influence the thermal structures and velocity fields of glaciers (e.g. Wilson et al., 2013; Zhang et al., 2015). However, in this study the removal of basal sliding (E-slip) results in a temperature field very similar to that of E-ref. We attribute this difference to the relatively small basal sliding values for LHG12. The observed and modelled ice temperature profiles of E-advZ, E-advX, E-strain, E-slip and E-ref are also compared for the deep ice borehole at site 3 in Fig. 9d.

4.5 Model limitations

Although our 2D, higher-order, first-order, flow-band model can account for part of the three-dimensional nature of LHG12 by parameterizing the lateral drag with glacier width variations, it cannot fully include the ice flow and heat advection along the y direction. For example, the convergent flow from the west branch could influence the modelled ice velocity from 6.3 km to the glacier terminus (Figs. 5 and 7b). The shape of the LHG12 glacier valley is described using a constant value for index b (1.2; approximately “V” type cross-sections), which was determined from several traverse GPR profiles (Fig. 1). However, for real glaciers, the cross-sectional geometry profiles are generally complex, resulting in an inevitable bias when we idealize the

The Cryosphere Discuss., doi:10.5194/tc-2016-38, 2016
Manuscript under review for journal The Cryosphere
Published: 4 March 2016

glacier cross-sectional profiles by using power law functions across the entire LHG12 area. Although the regularized Coulomb friction law provides a physically relationship between the basal drag and sliding velocities, several parameters (e.g., $\lambda_{\max}$, $m_{\max}$) still must be prescribed based on surface velocity observations.

Due to the limitations of *in situ* shallow borehole ice temperature measurements, the surface thermal boundary condition in our temperature model is determined using a simple interpolation method based on observations at three elevations (Fig. 1). In addition, the method presented by Wohlleben et al. (2009) that we follow here for determining the surface thermal boundary condition only provides a rough estimate of the overall contributions of the heat from refreezing melt-water and ice flow advection. At this stage, we cannot simulate the actual physical process involved in the transport of near-surface heat from refreezing, which has been suggested by Gilbert et al. (2012); Wilson and Flowers (2013). The assumption of steady state neglects the transient effects of past climate and glacier changes, which may have an impact on the shape of temperature profile (Gilbert et al., 2015).

5 Conclusions

For the first time, we investigate the thermo-mechanical features of a typical valley glacier, Laohugou No.12 Glacier (LHG12), on Mt. Qilian Shan, which is an important fresh water source for the arid regions in western China. We assess the present thermal status of LHG12 using a two-dimensional thermo-mechanically coupled first-order flow-band model using existing *in situ* measurements, e.g., glacier geometries, borehole ice temperatures, and surface meteorological and velocity observations. By carefully comparing modelled ice velocities and temperatures with *in situ* observations, we conduct a set of numerical sensitivity experiments that include, for example, basal sliding parameters, geothermal heat fluxes and glacial valley shapes. In addition, we investigate the impacts of different surface thermal conditions (surface air and near-surface ice temperatures), heat advection, strain heating and basal sliding on our numerical model results.

Similar to other alpine land-terminating glaciers, the mean annual horizontal ice flow speeds (u) of LHG12 are relatively low (less than 40 m a^{-1}). However, we observed large inter-annual variations in the ice surface velocity during the summer and winter seasons. Due to the release of heat from refreezing melt-water, the observed ice temperatures for the shallow ice borehole in the accumulation basin (site 3; Fig. 1) are higher than for the temperatures at sites 1 and 2 at lower elevations, indicating the existence of melt-water refreezing, as observed in our field expeditions. Thus, we constrain the thermal surface boundary condition by using the 20m deep ice temperatures instead of only the surface air temperatures. We observed that LHG12 has a polythermal structure with a temperate ice zone (approximately 5.4 km long) that is overlain by cold ice near the glacier base throughout a large region of the ablation area.

Horizontal heat advection is important on LHG12 for bringing the relatively warm ice in the accumulation basin (due to the heat from refreezing melt-water) to the downstream ablation zone. In addition, vertical heat advection is important for transporting the near-surface cold ice downwards into the glacier interior, which "cools down" the ice temperature. Furthermore, we argue that the strain heating of LHG12 plays the most important role in controlling the en-glacial thermal status, as suggested

The Cryosphere Discuss., doi:10.5194/tc-2016-38, 2016
Manuscript under review for journal The Cryosphere
Published: 4 March 2016

by Zhang et al. (2015). However, we also observed that basal sliding contributes little to the thermal-mechanical configuration of LHG12 (very small; < 4 m a^{-1}).

The mean annual surface air temperature could serve as a good approximation for the temperatures of shallow ice, where seasonal climate variations are damped at cold and dry locations (Cuffey and Paterson, 2010). However, for LHG12, using the mean annual surface air temperature as the thermal boundary condition at the ice surface would predict an entirely cold glacier with very small ice flow speeds. Because warming is occurring on alpine glaciers in, for example, Mt. Himalayas and Qilian Shan, further studies of supra-glacial and near-surface heat transport are very important because they will affect the surface thermal conditions and, eventually, the dynamical behaviours of the glacier.

Acknowledgements. This work is supported by the National Basic Research Program (973) of China (2013CBA01801, 2013CBA01804). We are grateful to numerous people for their hard fieldwork. We thank the supports from the Qilian Shan Station of Glaciology and Ecologic Environment, Chinese Academy of Sciences (CAS).

References

Blatter, H. and Greve, R.: Comparison and verification of enthalpy schemes for polythermal glaciers and ice sheets with a one-dimensional model, Polar Science, 9, 196–207, 2015.

Blatter, H. and Hutter, K.: Polythermal conditions in Arctic glaciers, Journal of Glaciology, 37, 261–269, 1991.

Cuffey, K. and Paterson, W.: The Physics of Glaciers, Elsevier, Amsterdam, 4^{th} edn., 2010.

Du, W., Qin, X., Liu, Y., and Wang, X.: Variation of the Laohugou Glacier No.12 in the Qilian Mountains, Journal of Glaciology and Geocryology, 30, 373–379, [In Chinese with English summary], 2008.

Flowers, G. E., Roux, N., Pimentel, S., and Schoof, C. G.: Present dynamics and future prognosis of a slowly surging glacier, The Cryosphere, 5, 299–313, 2011.

Funk, M., Echelmeyer, K. A., and Iken, A.: Mechanisms of fast flow in Jakobshavn Isbræ, West Greenland: Part II. Modeling of englacial temperatures, Journal of Glaciology, 40, 569–585, 1994.

Gagliardini, O., Cohen, D., Råback, P., and Zwinger, T.: Finite-element modeling of subglacial cavities and related friction law, Journal of Geophysical Research, 112, 2007.

Gilbert, A., Vincent, C., Wagnon, P., Thibert, E., and Rabatel, A.: The influence of snow cover thickness on the thermal regime of Tête Rousse Glacier (Mont Blanc range, 3200 m a.s.l.): Consequences for outburst flood hazards and glacier response to climate change, Journal of Geophysical Research, 117, 2012.

Gilbert, A., Vincent, C., Gagliardini, O., Krug, J., and Berthier, E.: Assessment of thermal change in cold avalanching glaciers in relation to climate warming, Geophysical Research Letters, 42, 6382–6390, 2015.

Guo, W., Xu, J., Liu, S., Shangguan, D., Wu, L., Yao, X., Zhao, J., Liu, Q., Jiang, Z., Li, P., Wei, J., Bao, W., Yu, P., Ding, L., Li, G., Ge, C., and Wang, Y.: The second glacier inventory dataset of China (Version 1.0), Cold and Arid Regions Science Data Center at Lanzhou, 2014.

Guo, W., Liu, S., Xu, J., Wu, L., Shangguan, D., Yao, X., Wei, J., Bao, W., Yu, P., Liu, Q., and Jiang, Z.: The second Chinese glacier inventory: data, methods and results, Journal of Glaciology, 61, 357–372, 2015.

Huang, M.: On the temperature distribution of glaciers in China, Journal of Glaciology, 36, 210–216, 1990.

Huang, M.: Forty year's study of glacier temperature in China, Journal of Glaciology and Geocryology, 21, 193–199, [In Chinese with English summary], 1999.

Huang, M., Wang, Z., and Ren, J.: On the temperature regime of continental-type glaciers in China, Journal of Glaciology, 28, 117–128, 1982.

Huss, M., Jouvet, G., Farinotti, D., and Bauder, A.: Future high-mountain hydrology: a new parameterization of glacier retreat, Hydrology and Earth System Sciences, 14, 815–829, 2010.

Irvine-Fynn, T. D. L., Hodson, A. J., Moorman, B. J., Vatne, G., and Hubbard, A. L.: Polythermal glacier hydrology: A review, Reviews of Geophysics, 49, 2011.

Jansson, P., Hock, R., and Schneider, T.: The concept of glacier storage: a review, Journal of Hydrology, 282, 116–129, 2003.

Liu, Y., Qin, X., Du, W., Sun, W., and Hou, D.: The movement features analysis of Laohugou Glacier No.12 in Qilian Mountains, Sciences in Cold and Arid Regions, 3, 119–123, 2011.

Meierbachtol, T. W., Harper, J. T., Johnson, J. V., Humphrey, N. F., and Brinkerhoff, D. J.: Thermal boundary conditions on western Greenland: Observational constraints and impacts on the modeled thermomechanical state, Journal of Geophysical Research: Earth Surface, 120, 623–636, 2015.

Neckel, N., Kropáček, J., Bolch, T., and Hochschild, V.: Glacier mass changes on the Tibetan Plateau 2003–2009 derived from ICESat laser altimetry measurements, Environmental research letters, 9, 014 009, 2014.

Pattyn, F.: Transient glacier response with a higher-order numerical ice-flow model, Journal of Glaciology, 48, 467–477, 2002.

Schäfer, M., Gillet-Chaulet, F., Gladstone, R., Pettersson, R., A. Pohjola, V., Strozzi, T., and Zwinger, T.: Assessment of heat sources on the control of fast flow of Vestfonna ice cap, Svalbard, The Cryosphere, 8, 1951–1973, 2014.

Schoof, C.: The effect of cavitation on glacier sliding, Royal Society of London Proceedings Series A, 461, 609–627, 2005.

Shi, Y. and Liu, S.: Estimation on the response of glaciers in China to the global warming in the 21st century, Chinese Science Bulletin, 45, 668–672, 2000.

Sugiyama, S., Sakakibara, D., Matsuno, S., Yamaguchi, S., Matoba, S., and Aoki, T.: Initial field observations on Qaanaaq ice cap, northwestern Greenland, Annals of Glaciology, 55, 25–33, 2014.

Sun, W., Qin, X., Ren, J., Yang, X., Zhang, T., Liu, Y., Cui, X., and Du, W.: The surface energy budget in the accumulation zone of the Laohugou Glacier No.12 in the western Qilian Mountains, China, in summer 2009, Arctic, Antarctic, and Alpine Research, 44, 296–305, 2012.

Svensson, H.: Is the cross-section of a glacial valley a parabola?, Journal of Glaciology, 3, 362–363, 1959.

Tian, H., Yang, T., and Liu, Q.: Climate change and glacier area shrinkage in the Qilian Mountains, China, from 1956 to 2010, Annals of Glaciology, 55, 187–197, 2014.

Van der Veen, C. J.: A numerical scheme for calculating stresses and strain rates in glaciers, Mathematical geology, 21, 363–377, 1989.

Wang, Y., Ren, J., Qin, X., Liu, Y., Zhang, T., Chen, J., Li, Y., and Qin, D.: Ice thickness and glacier-bed characteristics of Laohugou No.12 Glacier, Qilian Mountains from ground-penetrating radar, Journal of Glaciology and Geocryology, [In Chinese with English summary], in press.

Wilson, N. J. and Flowers, G. E.: Environmental controls on the thermal structure of alpine glaciers, The Cryosphere, 7, 167–182, 2013.

Wilson, N. J., Flowers, G. E., and Mingo, L.: Comparison of thermal structure and evolution between neighboring subarctic glaciers, Journal of Geophysical Research: Earth Surface, 118, 1443–1459, 2013.

Wohlleben, T., Sharp, M., and Bush, A.: Factors influencing the basal temperatures of a High Arctic polythermal glacier, Annals of Glaciology, 50, 9–16, 2009.

Yao, T., Thompson, L., Yang, W., Yu, W., Gao, Y., Guo, X., Yang, X., Duan, K., Zhao, H., and Xu, B.: Different glacier status with atmospheric circulations in Tibetan Plateau and surroundings, Nature Climate Change, 2, 663–667, 2012.

Zhang, T., Xiao, C., Colgan, W., Qin, X., Du, W., Sun, W., Liu, Y., and Ding, M.: Observed and modelled ice temperature and velocity along the main flowline of East Rongbuk Glacier, Qomolangma (Mount Everest), Himalaya, Journal of Glaciology, 59, 438–448, 2013.

Zhang, T., Ju, L., Leng, W., Price, S., and Gunzburger, M.: Thermomechanically coupled modelling for land-terminating glaciers: a comparison of two-dimensional, first-order and three-dimensional, full-Stokes approaches, Journal of Glaciology, 61, 702–712, 2015.

The Cryosphere Discuss., doi:10.5194/tc-2016-38, 2016
Manuscript under review for journal The Cryosphere
Published: 4 March 2016

Table 1. Parameters used in this study

Symbol	Description	Value	Unit
β	Clausius-Clapeyron constant	8.7×10^{-4}	K m^{-1}
g	Gravitational acceleration	9.81	m s^{-2}
ρ	Ice density	910	kg m^{-3}
ρ_w	Water density	1000	kg m^{-3}
n	Exponent in Glen's flow law	3	-
$\dot{\epsilon}_0$	viscosity regularization	10^{-30}	a^{-1}
A_0	Flow law parameter		
	when T $\leq$ 263.15 K	3.985×10^{-13}	Pa^{-3} s^{-1}
	when T $>$ 263.15 K	1.916×10^{3}	Pa^{-3} s^{-1}
Q	Creep activation energy		
	when T $\leq$ 263.15 K	60	kJ mol^{-1}
	when T $>$ 263.15 K	139	kJ mol^{-1}
R	Universal gas constant	8.31	J mol^{-1} K^{-1}
k	Thermal conductivity	2.1	W m^{-1} K^{-1}
c_p	Heat capacity of ice	2009	J kg^{-1} K^{-1}
L	Latent heat of fusion of ice	3.35×10^{-5}	J kg^{-1}
T_0	Triple-point temperature of water	273.16	K

The Cryosphere Discuss., doi:10.5194/tc-2016-38, 2016
Manuscript under review for journal The Cryosphere
Published: 4 March 2016

The Cryosphere Discussions

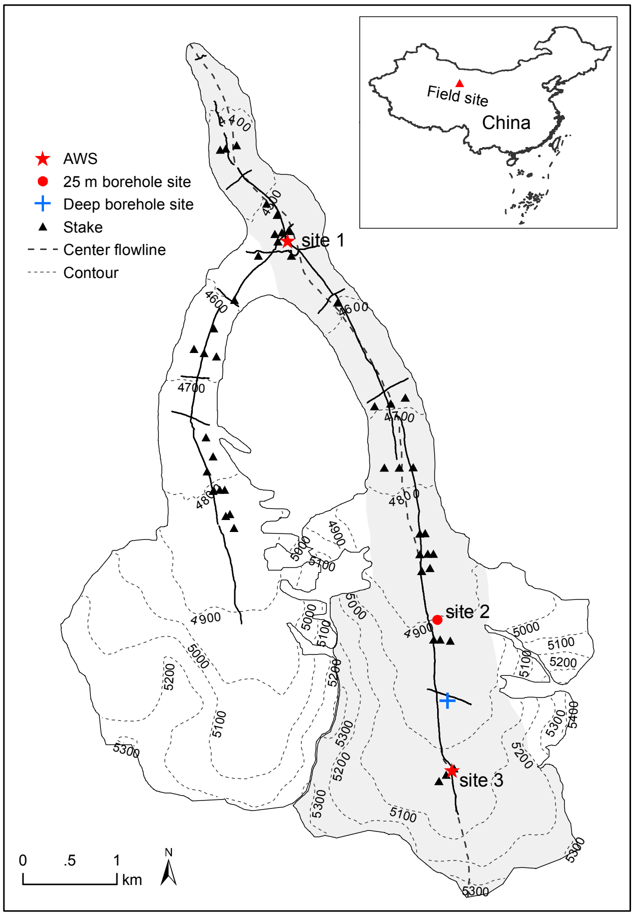

Figure 1. Map of LHG12. The solid and thick black lines indicate the GPR survey lines. The shaded area denotes the mainstream of LHG12, which only includes the east branch and neglects the west branch and all small tributaries. The dashed black line represents the center flowline. Red stars indicate the locations of the automatic weather stations and the 25m deep shallow boreholes (sites 1 and 3). A solid red circle represents the location of the shallow borehole at site 2, and a blue cross represents the location of the deep ice borehole. Black triangles show the positions of the stakes used for ice surface velocity measurements. The contours were generated from SRTM DEM in 2000.

The Cryosphere Discuss., doi:10.5194/tc-2016-38, 2016
Manuscript under review for journal The Cryosphere
Published: 4 March 2016

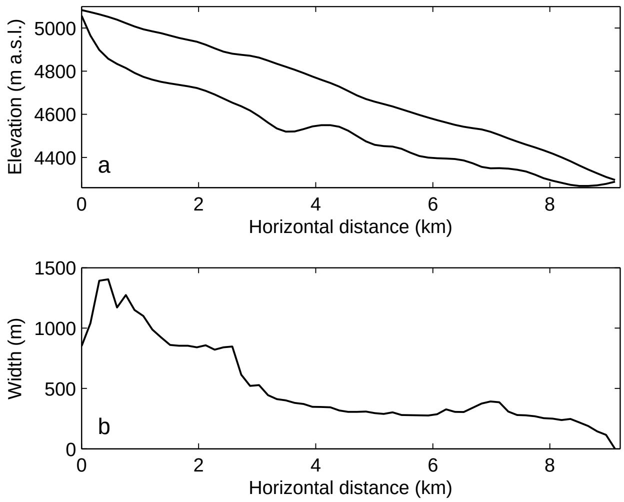

Figure 2. (a) Glacier surface and bed topography along the center flow-line. (b) Glacier widths along the center flow-line.

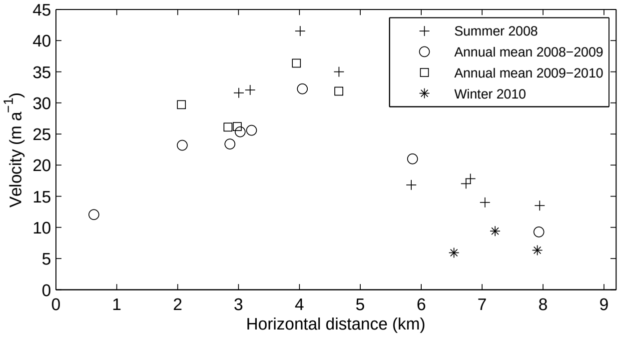

Figure 3. Measured ice surface velocities along the center flow-line.

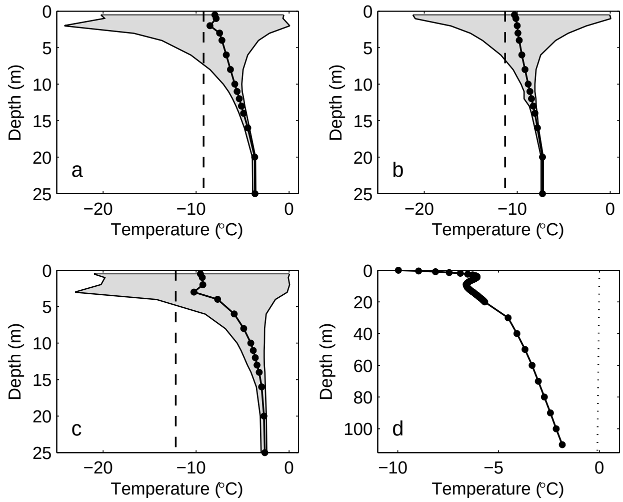

Figure 4. Ice temperature measurements from the four ice boreholes. (a, b, c) Ice temperature measurements from the 25m deep boreholes at sites 1, 2, and 3, respectively. The black dots show the mean annual ice temperatures over the period of 2010 – 2011. The shaded areas show the yearly fluctuation range of the ice temperature. The dashed lines indicate the mean annual air temperature. (d) Measured ice temperatures from the deep borehole. The dotted line denotes the pressure-melting point (PMP) as a function of elevation.

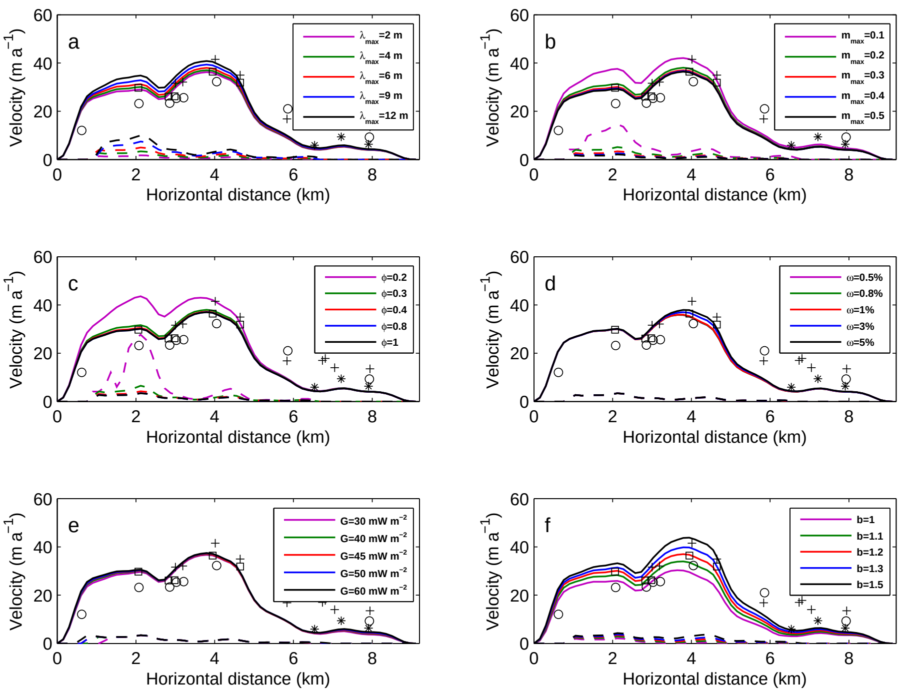

Figure 5. The sensitivity of the modelled ice flow speeds to parameters along the CL. The solid and dashed lines indicate the modelled surface and basal sliding velocities, respectively. Symbols show the measured ice surface velocities (see Fig. 3).

The Cryosphere Discuss., doi:10.5194/tc-2016-38, 2016
Manuscript under review for journal The Cryosphere
Published: 4 March 2016

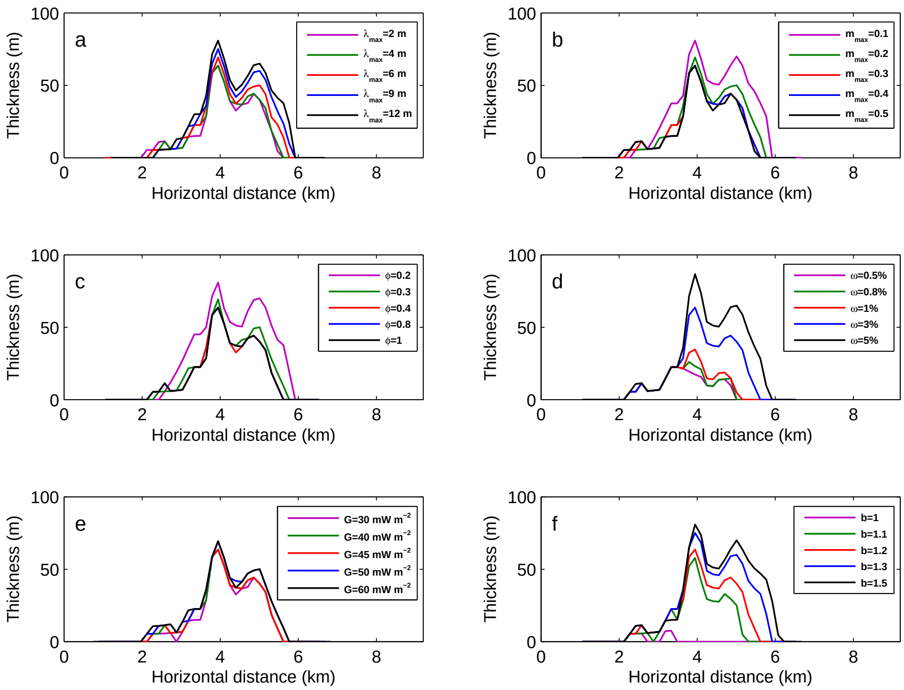

Figure 6. The sensitivity of the modelled temperate ice thicknesses to parameters along the CL. The parameter settings are same as those described in Fig. 5.

The Cryosphere Discuss., doi:10.5194/tc-2016-38, 2016
Manuscript under review for journal The Cryosphere
Published: 4 March 2016

The Cryosphere
Discussions
Open Access

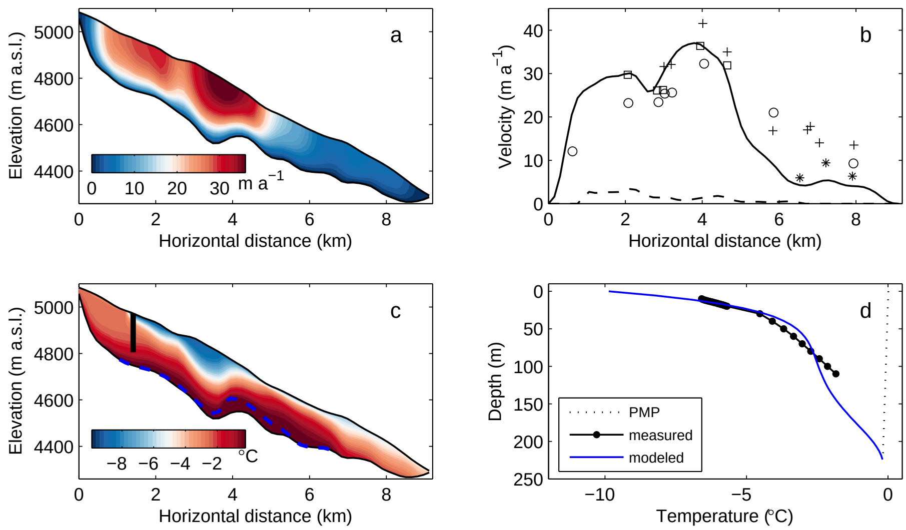

Figure 7. A comparison of the modelled and measured ice temperatures and horizontal velocities (u). (a) The distribution of the modelled horizontal ice velocity (u). (b) Measured (symbols) and modelled (solid line) surface and basal (dashed line) horizontal velocities. The symbols are the same as described in Fig. 3. (c) The distribution of the modelled ice temperature. The blue dashed line indicates the CTS position, and the black bar shows the location of the deep ice borehole. (d) Modeled (blue line) and measured (dots) ice temperature profiles for the deep borehole. The pressure-melting point is shown by the dotted line.

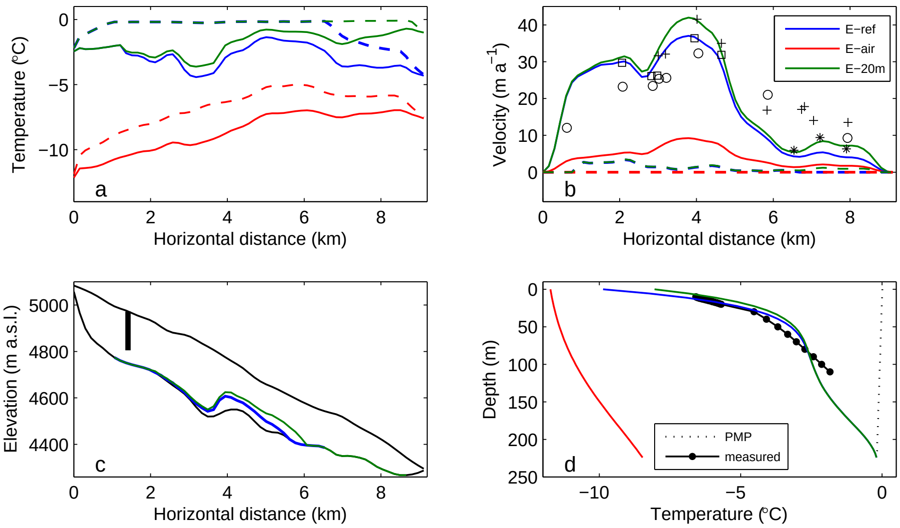

Figure 8. Modeled ice temperatures and velocities for experiments E-ref (blue line), E-air (red line), and E-20m (green line). (a) Modeled column mean (solid lines) and basal (dashed lines) ice temperatures along the CL. (b) Modeled surface (solid lines) and basal (dashed lines) ice velocities along the CL. The symbols for the measured ice surface velocities are the same as those shown in Fig. 3. (c) Modeled CTS position. The black bar shows the location of the deep ice borehole. (d) Measured (coloured lines) and modelled (dots) ice temperature profiles for the deep borehole. The dotted line shows the pressure-melting point as a function of ice depth.

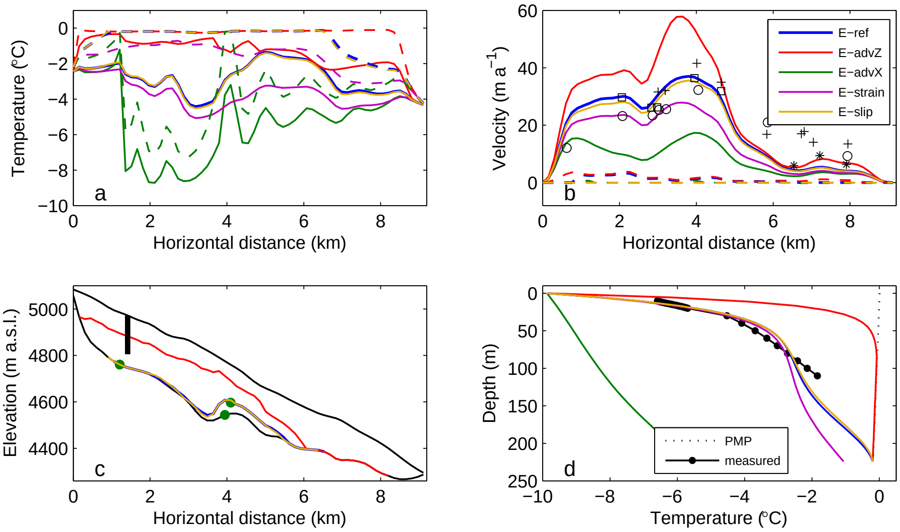

Figure 9. Modeled ice temperatures and velocities for experiments E-ref (blue line), E-advZ (red line), E-advX (green line), E-strain (purple line), and E-slip (yellow line). (a) Modeled column mean (solid lines) and basal (dashed lines) ice temperatures along the CL. (b) Modeled surface (solid lines) and basal (dashed lines) ice velocities along the CL. The symbols for the measured ice surface velocities are the same as those shown in Fig. 3. (c) Modeled CTS position. The black bar shows the location of the deep ice borehole. (d) Measured (coloured lines) and modelled (dots) ice temperature profiles for the deep borehole. The dotted line shows the pressure-melting point as a function of ice depth.